

MASTER THESIS & STUDENT PROJECT

Density Upwinding in Finite Element Full-Potential Flow Solver

Eloisa Baez Jones



Chair of Structural Analysis
Prof. Dr.-Ing. K.-U. Bletzinger
Technical University of Munich

Technische Universität München

Department of Civil Engineering

Chair of Structural Analysis

Density Upwinding in Finite-Element Full-Potential Flow Solver

Master's Thesis and Student Project in Computational Mechanics

Eloisa Baez Jones

Matr.-Nr.

Thesis Advisor
Dr.-Ing. Roland Wüchner

Thesis Advisor
Íñigo López Canalejo

Chair of Structural Analysis
Prof. Dr.-Ing. Kai-Uwe Bletzinger

Munich, May 8, 2020

Abstract

Acknowledgments

Contents

Abstract	IV
Acknowledgments	VI
Contents	VII
1 Introduction	2
1.1 Motivation	2
2 Incompressible Potential Flow	3
2.1 Finite Element Derivation	3
3 Subsonic Compressible Potential Flow	6
3.1 Finite Element Derivation	6
4 Transonic Compressible Potential Flow	9
4.1 Finite Element Derivation	9
4.2 Implementation in Kratos	12
4.2.1 Clamping Values	13
4.2.2 Upwind Element Search	14
5 Validation and Verification of Incompressible Potential Flow	19
6 Validation and Verification of Subsonic Compressible Potential Flow	21
6.1 Mesh Refinement	22
6.1.1 Verification	22
6.1.2 Validation	27
6.2 Domain Study	30
6.2.1 Verification	30
6.2.2 Validation	31
7 Validation and Verification of Transonic Compressible Potential Flow	40
8 Conclusions	42
8.1 Summary	42
8.2 Outlook	42
Appendix	44
Bibliography	46
Declaration	48

1 Introduction

1.1 Motivation

2 Incompressible Potential Flow

2.1 Finite Element Derivation

In order to derive with the stiffness matrix for an incompressible potential flow element, we begin with the residual formulation of the stiffness matrix in Eq. 2.1. An explanation of the meaning behind the indices in this derivation can be seen in Table 2.1, and a schematic of an example element's nodes can be seen in Fig. 2.1.

$$\mathbf{K} = \frac{\partial \mathbf{R}}{\partial \Phi} = \frac{\partial R^i}{\partial q^a} \frac{\partial q^b}{\partial \Phi^j} \quad (2.1)$$

Table 2.1: Guide to Index Notation in Derivation

Notation	Description	Components
i	indices in parameter space	$[\xi_1, \xi_2, \xi_3]$
j	element nodes	[1, 2, 3]
a, b	indices in physical space	[x, y]

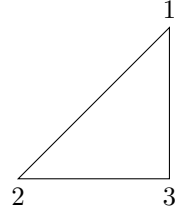


Figure 2.1: Schematic of an element's nodes

The residual is defined as in Eq. 2.2. This can then be reduced to Eq. 2.3 as we are only working in two dimensions and the second part of the residual corresponds to a Neumann boundary condition which is not relevant to the flow cases studied here.

$$R^i = \int \int \int_V \frac{\partial N^i}{\partial x^a} (\rho q^a) dV - \int \int_S N^i (\rho q^a) n^a dS \quad (2.2)$$

$$R^i = \int \int_S \frac{\partial N^i}{\partial x^a} (\rho q^a) dS \quad (2.3)$$

Then the derivative of the residual is:

$$\frac{\partial R^i}{\partial q^a} = \int \int_S \frac{\partial N^i}{\partial x^a} (\rho) dS \quad (2.4)$$

The velocity is defined as in Eq. 2.5. Which then leads to the derivative in Eq. 2.6.

$$q^b = q_\infty + \frac{\partial N^j}{\partial x^b} \Phi^j \quad (2.5)$$

$$\frac{\partial q^a}{\partial \Phi^j} = \frac{\partial N^j}{\partial x^a} \quad (2.6)$$

Then Eq. 2.7 gives the definition of the element stiffness matrix for an incompressible potential flow element. To further illustrate the meaning of the indices, the shape function matrices are written out in full in Eq. 2.8.

$$K^{ij} = \frac{\partial R^i}{\partial q^a} \frac{\partial q^b}{\partial \Phi^j} = \int \int_S \frac{\partial N^i}{\partial x^a} \frac{\partial N^j}{\partial x^b} \rho dS \quad (2.7)$$

$$\frac{\partial N^i}{\partial x^a} \frac{\partial N^j}{\partial x^b} = \nabla N_i \cdot \nabla N_j = \begin{bmatrix} \frac{\partial N^1}{\partial x} & \frac{\partial N^1}{\partial y} \\ \frac{\partial N^2}{\partial x} & \frac{\partial N^2}{\partial y} \\ \frac{\partial N^3}{\partial x} & \frac{\partial N^3}{\partial y} \end{bmatrix} \cdot \begin{bmatrix} \frac{\partial N^1}{\partial x} & \frac{\partial N^2}{\partial x} & \frac{\partial N^3}{\partial x} \\ \frac{\partial N^1}{\partial y} & \frac{\partial N^2}{\partial y} & \frac{\partial N^3}{\partial y} \end{bmatrix} \quad (2.8)$$

3 Subsonic Compressible Potential Flow

3.1 Finite Element Derivation

In order to derive with the stiffness matrix for a subsonic compressible potential flow element, we begin again with the residual formulation of the stiffness matrix in Eq. 3.1. The crucial difference now is that the density is not taken as a constant but as defined in Eq. 3.2.

$$\mathbf{K} = \frac{\partial \mathbf{R}}{\partial \Phi} = \frac{\partial R^i}{\partial q^a} \frac{\partial q^b}{\partial \Phi^j} \quad (3.1)$$

$$\rho = \rho_\infty \left[1 + \frac{\gamma-1}{2} M_\infty^2 \left(1 - \frac{|q|^2}{q_\infty^2} \right) \right]^{\frac{1}{\gamma-1}} \quad (3.2)$$

The residual equation is the same as for the incompressible case however now the derivative of the residual changes as the density depends on the velocity as shown in Eq. 3.4.

$$R^i = \int \int_S \frac{\partial N^i}{\partial x^a} (\rho q^b) dS \quad (3.3)$$

$$\frac{\partial R^i}{\partial q^a} = \int \int_S \frac{\partial N^i}{\partial x^a} \left(\frac{\partial \rho}{\partial q^a} q^b + \rho \right) dS \quad (3.4)$$

The derivative of the density is defined as follows:

$$\frac{\partial \rho}{\partial q^a} = \frac{\partial \rho}{\partial |q|^2} \frac{\partial |q|^2}{\partial q^a} \quad (3.5)$$

$$\frac{\partial \rho}{\partial |q|^2} = -\frac{\rho_\infty M_\infty^2}{2 q_\infty^2} \left[1 + \frac{\gamma-1}{2} M_\infty^2 \left(1 - \frac{|q|^2}{q_\infty^2} \right) \right]^{\frac{2-\gamma}{\gamma-1}} \quad (3.6)$$

$$|q| = \sqrt{q^a q^a} \quad (3.7)$$

$$\frac{\partial |q|^2}{\partial q^a} = 2 q^a \quad (3.8)$$

Then the velocity and it's derivatives are also the same as for the incompressible case:

$$q^b = q_\infty + \frac{\partial N^j}{\partial x^b} \Phi^j \quad (3.9)$$

$$\frac{\partial q^a}{\partial \Phi^j} = \frac{\partial N^j}{\partial x^b} \quad (3.10)$$

Then the stiffness matrix for the subsonic compressible potential flow element is as in Eq. 3.12.

$$K^{ij} = \int \int_S \frac{\partial N^i}{\partial x^a} \frac{\partial N^j}{\partial x^b} \rho + \frac{\partial N^i}{\partial x^a} \frac{\partial N^j}{\partial x^b} \frac{\partial \rho}{\partial |q|^2} \frac{\partial |q|^2}{\partial q^a} q^b dS \quad (3.11)$$

$$K^{ij} = \int \int_S \frac{\partial N^i}{\partial x^a} \frac{\partial N^j}{\partial x^b} \rho + 2 \frac{\partial \rho}{\partial |q|^2} \left(\frac{\partial N^i}{\partial x^a} q^a q^b \frac{\partial N^j}{\partial x^b} \right) dS \quad (3.12)$$

4 Transonic Compressible Potential Flow

4.1 Finite Element Derivation

We begin again with the definition of our stiffness matrix according to the chain rule in Eq. 4.1. However, in order to accomodate higher Mach numbers the density is now modified as defined in Eq. 4.9. With this density modification, which we refer to as the upwinded density, the upwind element modifies the current element by their shared nodes as depicted by Fig. 4.1. This influence also leads to more nodes being considered, this effect on the notation of the derivation is explained in Table 4.1.

$$\mathbf{K} = \frac{\partial \mathbf{R}}{\partial \Phi} = \frac{\partial R^i}{\partial q_e^a} \frac{\partial q_e^b}{\partial \Phi^j} + \frac{\partial R^i}{\partial q_{up}^a} \frac{\partial q_{up}^b}{\partial \Phi^j} \quad (4.1)$$

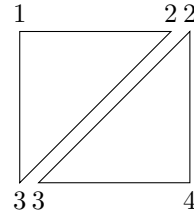


Figure 4.1: Schematic of an current element related to an upwind element and the shared nodes

Table 4.1: Guide to Index Notation in Derivation

Notation	Description	Components
i	indices in parameter space	$[\xi_1, \xi_2, \xi_3]$
j	current and upwind element nodes	$[1, 2, 3, 4]$
a, b	indices in physical space	$[x, y]$
e	current element	-
up	upwind element	-

The velocity and its derivatives remain the same except that the upwind element must also be taken into account.

$$q_e^b = q_\infty^b + \frac{\partial N_e^j}{\partial x_e^b} \Phi_e^j \quad (4.2)$$

$$\frac{\partial q_e^b}{\partial \Phi^j} = \frac{\partial N_e^j}{\partial x_e^b} \quad (4.3)$$

$$q_{up}^b = q_\infty^b + \frac{\partial N_{up}^j}{\partial x_{up}^b} \Phi^j \quad (4.4)$$

$$\frac{\partial q_{up}^b}{\partial \Phi^j} = \frac{\partial N_{up}^j}{\partial x_{up}^b} \quad (4.5)$$

The definition of the residual already reduced for two dimensions is in Eq. 4.6, except now the upwinded density, $\tilde{\rho}$, is used.

$$R^i = \int \int_S \frac{\partial N_e^i}{\partial x_e^a} \left(\tilde{\rho}_e q_e^b \right) dS \quad (4.6)$$

The derivative of the residual is as follows in Eq. 4.7 and Eq. 4.8.

$$\frac{\partial R^i}{\partial q_e^a} = \int \int_S \frac{\partial N_e^i}{\partial x_e^a} \left(\frac{\partial \tilde{\rho}_e}{\partial q_e^a} q_e^b + \tilde{\rho}_e \right) dS \quad (4.7)$$

$$\frac{\partial R^i}{\partial q_{up}^a} = \int \int_S \frac{\partial N_e^i}{\partial x_e^a} \left(\frac{\partial \tilde{\rho}_e}{\partial q_{up}^a} q_e^b \right) dS \quad (4.8)$$

The second part of the derivative of the residual refers to a Neumann boundary condition which is not relevant for the cases considered and is therefore neglected. In order to fully define Eq. 4.6 $\tilde{\rho}$ must be defined and its derivative must be defined:

$$\tilde{\rho}_e = \rho_e - \mu_f (\rho_e - \rho_{up}) \quad (4.9)$$

$$\frac{\partial \tilde{\rho}_e}{\partial q_e^a} = \frac{\partial \tilde{\rho}_e}{\partial |q|_e^2} \frac{\partial |q|_e^2}{\partial q_e^a} \quad (4.10)$$

$$\frac{\partial |q|_e^2}{\partial q_e^a} = 2 q_e^a \quad (4.11)$$

$$\frac{\partial \tilde{\rho}_e}{\partial |q|_e^2} = \frac{\partial \rho_e}{\partial |q|_e^2} - \left[\frac{\partial \mu_f}{\partial |q|_e^2} (\rho_e - \rho_{up}) + \mu_f \frac{\partial \rho_e}{\partial |q|_e^2} \right] \quad (4.12)$$

$$\frac{\partial \tilde{\rho}_e}{\partial q_{up}^a} = \frac{\partial \tilde{\rho}_e}{\partial |q|_{up}^2} \frac{\partial |q|_{up}^2}{\partial q_{up}^a} \quad (4.13)$$

$$\frac{\partial |q|_{up}^2}{\partial q_{up}^a} = 2 q_{up}^a \quad (4.14)$$

$$\frac{\partial \tilde{\rho}_e}{\partial |q|_{up}^2} = -\frac{\partial \mu_f}{\partial |q|_{up}^2} (\rho_e - \rho_{up}) + \mu_f \frac{\partial \rho_{up}}{\partial |q|_{up}^2} \quad (4.15)$$

The definition of the density and its derivative remain the same as in the subsonic case. Here the general case for either the upwind or current element is shown:

$$\rho = \rho_\infty \left[1 + \frac{\gamma-1}{2} M_\infty^2 \left(1 - \frac{|q|^2}{q_\infty^2} \right) \right]^{\frac{1}{\gamma-1}} \quad (4.16)$$

$$\frac{\partial \rho}{\partial |q|^2} = -\frac{\rho_\infty M_\infty^2}{2 q_\infty^2} \left[1 + \frac{\gamma-1}{2} M_\infty^2 \left(1 - \frac{|q|^2}{q_\infty^2} \right) \right]^{\frac{2-\gamma}{\gamma-1}} \quad (4.17)$$

In order to fully define $\tilde{\rho}$, μ_f and its derivatives must also be defined:

$$\mu_f = \max \begin{cases} 0 \\ \mu_c (1 - M_{crit}^2/M_e^2) \\ \mu_c (1 - M_{crit}^2/M_{up}^2) \end{cases} \quad (4.18)$$

The effect of the different cases can be seen below:

Table 4.2: Upwinding Factor Cases

	Case 1	Case 2	Case 3
Derivatives	$\mu_f = 0$	$\mu_f = \mu_c (1 - M_{crit}^2/M_e^2)$	$\mu_f = \mu_c (1 - M_{crit}^2/M_{up}^2)$
$\frac{\partial \mu_f}{\partial q _e^2}$	0	$\frac{\partial \mu_f}{M_e^2} \frac{\partial M_e^2}{\partial q _e^2}$	0
$\frac{\partial \mu_f}{M_e^2}$	0	$\mu_c \frac{M_{crit}^2}{M_e^4}$	0
$\frac{\partial \mu_f}{\partial q _{up}^2}$	0	0	$\frac{\partial \mu_f}{M_{up}^2} \frac{\partial M_{up}^2}{\partial q _{up}^2}$
$\frac{\partial \mu_f}{M_{up}^2}$	0	0	$\mu_c \frac{M_{crit}^2}{M_{up}^4}$

In order to fully define the derivative of μ_e the Mach number and its derivatives are also needed:

$$M^2 = M_\infty^2 \frac{|q|^2}{q_\infty^2} \left[1 + \frac{\gamma-1}{2} M_\infty^2 \left(1 - \frac{|q|^2}{q_\infty^2} \right) \right]^{-1} \quad (4.19)$$

$$Q = 1 + \frac{\gamma-1}{2} M_\infty^2 \left(1 - \frac{|q|^2}{q_\infty^2} \right) \quad (4.20)$$

$$M^2 = M_\infty^2 \frac{|q|^2}{q_\infty^2} Q^{-1} \quad (4.21)$$

$$\frac{\partial M^2}{\partial |q|^2} = M_\infty^2 \left[\frac{1}{q_\infty^2} Q^{-1} + \frac{|q|^2}{q_\infty^4} \frac{\gamma-1}{2} M_\infty^2 Q^{-2} \right] \quad (4.22)$$

$$\frac{\partial M^2}{\partial |q|^2} = M_\infty^2 \frac{|q|^2}{q_\infty^2} Q^{-1} \left[\frac{1}{|q|^2} + \frac{\gamma-1}{2} \frac{1}{q_\infty^2} M_\infty^2 Q^{-1} \right] \quad (4.23)$$

So the element and upwind element derivatives are:

$$\frac{\partial M_e^2}{\partial |q|_e^2} = M_e^2 \left[\frac{1}{|q|_e^2} + \frac{\gamma-1}{2} \frac{1}{q_\infty^2} M_\infty^2 Q_e^{-1} \right] \quad (4.24)$$

$$\frac{\partial M_{up}^2}{\partial |q|_{up}^2} = M_{up}^2 \left[\frac{1}{|q|_{up}^2} + \frac{\gamma-1}{2} \frac{1}{q_\infty^2} M_\infty^2 Q_{up}^{-1} \right] \quad (4.25)$$

This gives us all the necessary information to solve for the stiffness matrix by:

$$K_{ij} = \frac{\partial R^i}{\partial q_e^a} \frac{\partial q_e^b}{\partial \Phi^j} + \frac{\partial R^i}{\partial q_{up}^a} \frac{\partial q_{up}^b}{\partial \Phi^j} \quad (4.26)$$

$$= \int \int_S \frac{\partial N_e^i}{\partial x_e^a} \frac{\partial N_e^j}{\partial x_e^b} \left(\frac{\partial \tilde{\rho}_e}{\partial q_e^a} q_e^b + \tilde{\rho}_e \right) dS + \int \int_S \frac{\partial N_e^i}{\partial x_e^a} \frac{\partial N_{up}^j}{\partial x_{up}^b} \left(\frac{\partial \tilde{\rho}_e}{\partial q_{up}^a} q_e^b \right) dS \quad (4.27)$$

$$= \int \int_S \frac{\partial N_e^i}{\partial x_e^a} \frac{\partial N_e^j}{\partial x_e^b} \left(\frac{\partial \tilde{\rho}_e}{\partial |q|_e^2} \frac{\partial |q|_e^2}{\partial q_e^a} q_e^b + \tilde{\rho}_e \right) + \frac{\partial N_e^i}{\partial x_e^a} \frac{\partial N_{up}^j}{\partial x_{up}^b} \left(\frac{\partial \tilde{\rho}_e}{\partial |q|_{up}^2} \frac{\partial |q|_{up}^2}{\partial q_{up}^a} q_e^b \right) dS \quad (4.28)$$

$$= \int \int_S \frac{\partial N_e^i}{\partial x_e^a} \frac{\partial N_e^j}{\partial x_e^b} \tilde{\rho}_e + 2 \frac{\partial \tilde{\rho}_e}{\partial |q|_e^2} \left(\frac{\partial N_e^i}{\partial x_e^a} q_e^a q_e^b \frac{\partial N_e^j}{\partial x_e^b} \right) + 2 \frac{\partial \tilde{\rho}_e}{\partial |q|_{up}^2} \left(\frac{\partial N_e^i}{\partial x_e^a} q_e^a q_e^b \frac{\partial N_{up}^j}{\partial x_{up}^b} \right) dS \quad (4.29)$$

$$= \int \int_S \frac{\partial N_e^i}{\partial x_e^a} \frac{\partial N_e^j}{\partial x_e^b} \tilde{\rho}_e + 2 \frac{\partial N_e^i}{\partial x_e^a} q_e^a \left[\frac{\partial \tilde{\rho}_e}{\partial |q|_e^2} \left(q_e^b \frac{\partial N_e^j}{\partial x_e^b} \right) + \frac{\partial \tilde{\rho}_e}{\partial |q|_{up}^2} \left(q_{up}^b \frac{\partial N_{up}^j}{\partial x_{up}^b} \right) \right] dS \quad (4.30)$$

4.2 Implementation in Kratos

- how the inlet elements are handled
- how the [3 x 4] matrix is turned into a [4 x 4] matrix
- clamping values

4.2.1 Clamping Values

In addition to modifying the density by upwinding the density, Mach number, and speed of sound must also be clamped. This is because for some local velocities the these terms approach values which have no physical meaning. This most likely happens as the potential flow formulation still has limitations from the assumptions taken, especially the one of isentropic flow, which are noticeable at the local velocities. In order to visualize this issue first the speed of sound and density are calculated following Drela [1] as in Eq. 4.31 and Eq. 4.32. Then the Mach number can be formulated as in Eq. 4.33.

$$a^2 = a_\infty^2 \left[1 + \frac{\gamma-1}{2} M_\infty^2 \left(1 - \frac{|q|^2}{q_\infty^2} \right) \right] \quad (4.31)$$

$$\rho = \rho_\infty \left[1 + \frac{\gamma-1}{2} M_\infty^2 \left(1 - \frac{|q|^2}{q_\infty^2} \right) \right]^{\frac{1}{\gamma-1}} \quad (4.32)$$

$$M^2 = \frac{|q|^2}{a^2} \quad (4.33)$$

How these terms look for a range of local velocities can be seen in the first column Fig. 4.2. As can be seen, the all terms show physically unrealistic values such as the squared speed of sound becoming negative. Therefore it is chosen to clamp the square of the local Mach number to **3.0**. From this the maximum allowed velocity can also be calculated from this maximum value based on Eq. 4.34 and from this the velocity is clamped, and all terms are then calculated with the clamped velocity. The effect on the terms can then be seen in the second column of Fig. 4.2.

$$|q|^2 = M^2 q_\infty^2 \frac{M_\infty^2 \gamma - M_\infty^2 + 2}{M_\infty^2 \gamma M^2 - M^2 M_\infty^2 + 2 M_\infty^2} \quad (4.34)$$

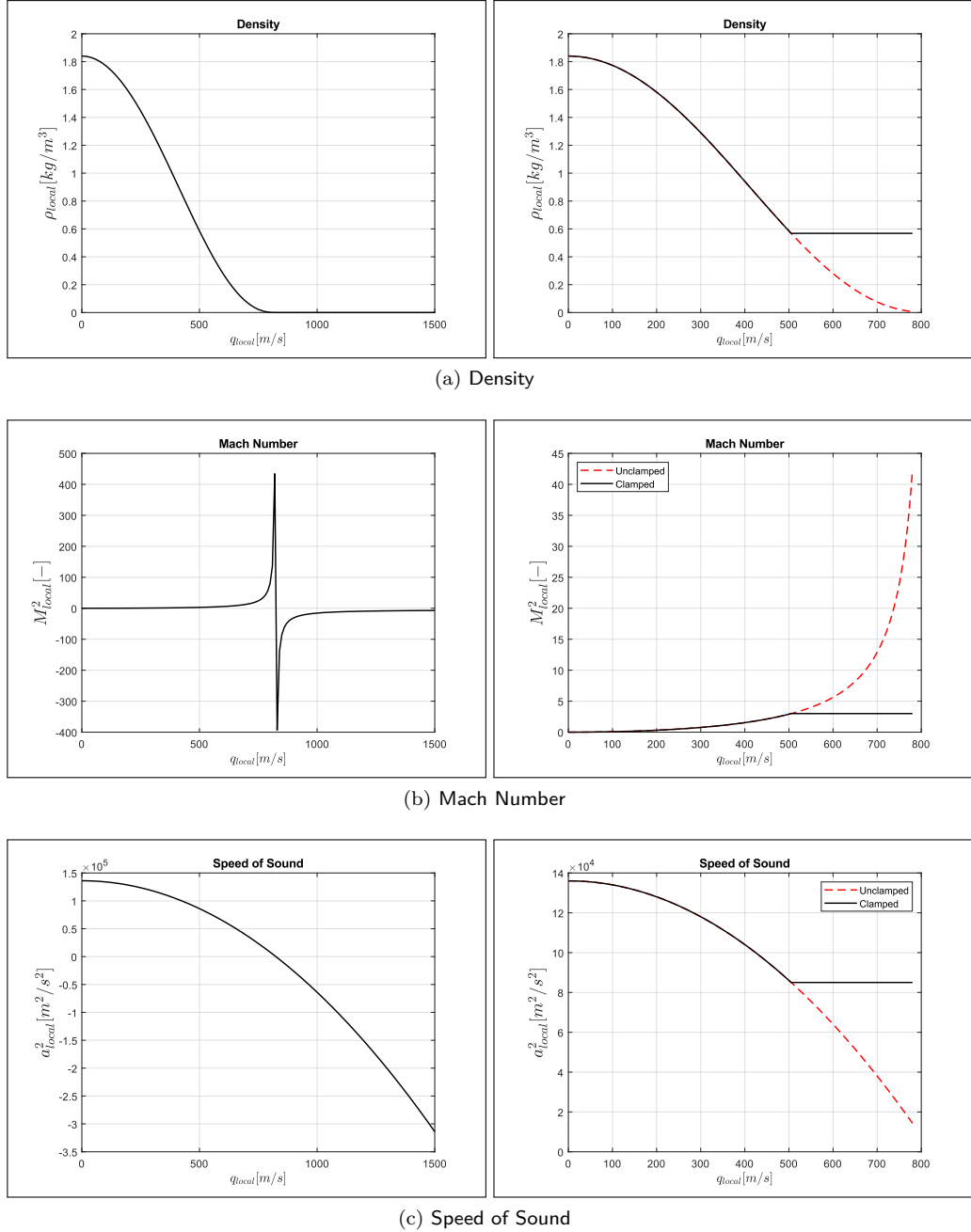


Figure 4.2: Effect of Clamping on Flow Values

4.2.2 Upwind Element Search

In order to decide on how to upwind the density the values from the upwind element must be known. Therefore a decision must be made on how to define the upwind element. First the upwind element is taken as one of the elements which shares an edge with our current element and therefore also shares two nodes with our current element. The other criteria defines a relationship between the element geometry and the free stream velocity direction.

As we want the element which has the fluid flow leaving its own boundary and flowing into our current element, we can say that the outward pointing vector normal to the edge of the upwind element which

is shared by our current element should point approximately in the same direction as the free stream velocity.

Therefore for our current element three normal vectors to the edges are calculated which point inward to our element (the same as vectors pointing out from the elements which share an edge). The normal is calculated by taking the cross product of the edge vectors, \vec{E} , and the z-axis vector.

$$\vec{N} = \begin{vmatrix} \hat{i} & \hat{j} & \hat{k} \\ E_x & E_y & E_z \\ 0 & 0 & 1 \end{vmatrix} \quad (4.35)$$

The element nodes are always labeled counterclockwise which enables us to get the inward pointing normal vectors by making the edge vectors clockwise. Meaning that the element edge vectors are drawn from point 2 to point 1, from point 3 to point 2 and from point 3 to point 1. The orientation of vectors used can be seen in Fig. 4.3.

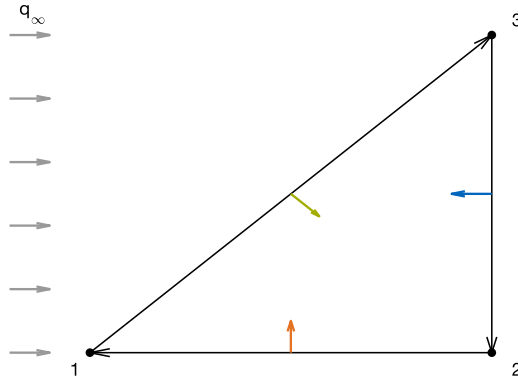


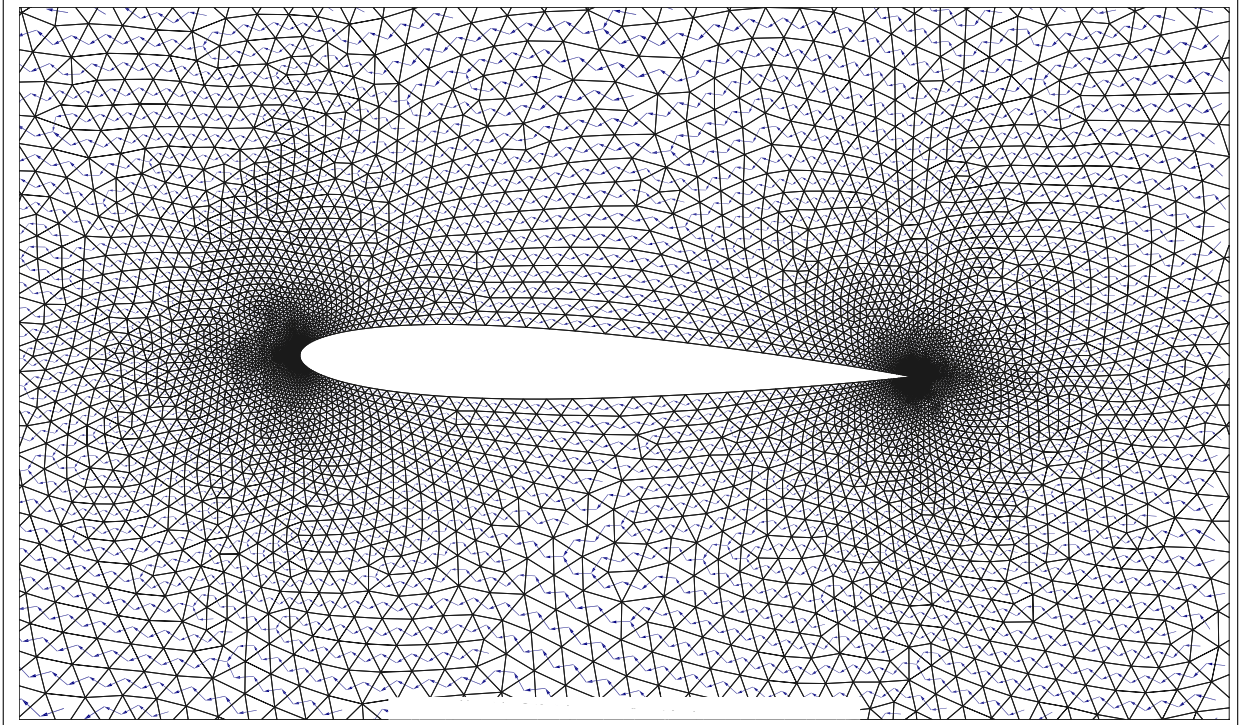
Figure 4.3: Schematic Showing Orientation of Normal Vectors of Element

Then the component of the normal vector in the free stream velocity vector direction is taken using the dot product. Then the largest component from the three edge normal vectors is selected, which should correspond to the element whose normal vector points most in the free stream velocity direction. As then the nodes corresponding to this vector with the maximum free stream component are known the list of all the elements attached to this node can be found. So a list of all attached elements for each node is made and the element which is attached to both nodes is saved as the upwind element.

$$\frac{\vec{N} \cdot \vec{q}_\infty}{|\vec{q}_\infty|} \quad (4.36)$$

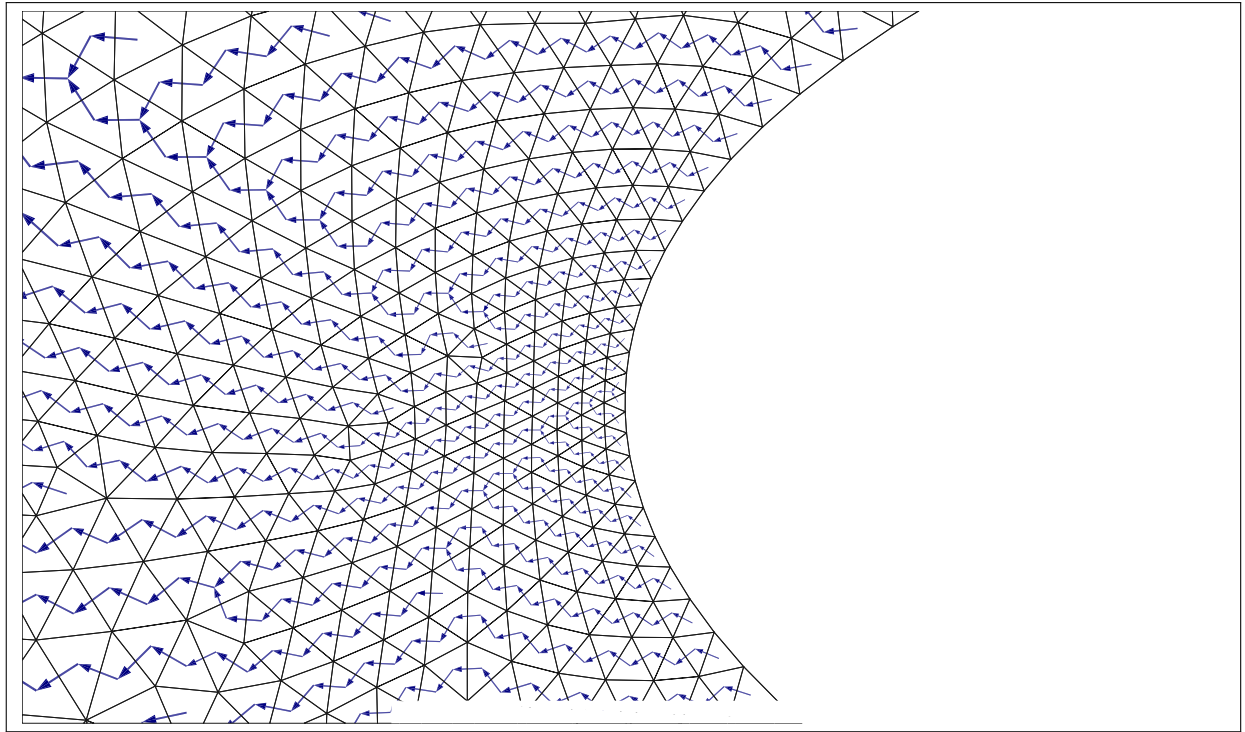
A vector is made which points from the center of the current element to the center of the element chosen as its upwind element. Saved under variable VECTOR_TO_UPWIND_ELEMENT. The result of this can be seen in Fig. 4.4 and 4.5. Note that the inlet elements on the have no vector. Currently the inlet

elements are not assigned an upwind element.



(a) Airfoil

Figure 4.4: Vector from Element to Corresponding Upwind Element for a NACA0012 airfoil with an angle of attack of 2° , a mesh size of 0.001, and a domain size of 100



(a) Leading Edge of Airfoil

Figure 4.5: Vector from Element to Corresponding Upwind Element for a NACA0012 airfoil with an angle of attack of 2° , a mesh size of 0.001, and a domain size of 100

5 Validation and Verification of Incompressible Potential Flow

6 Validation and Verification of Subsonic Compressible Potential Flow

Validation and verification of simulation software is an important development step. Verification checks that the software implementation returns expected values checking for errors both in the implementation of the physical model and programming errors. Validation checks that the implementation sufficiently represents the physical situation. Here the verification and validation of the full potential solver is presented for compressible subsonic flows. Compressible flows are characterized by significant changes in density in the flow [1]. Typically a flow is taken to be compressible once the Mach number is above 0.3 where the Mach number is defined as in Eq. 6.1. Subsonic flows mean the flow is slower than the speed of sound giving a Mach number smaller than one.

$$M = \frac{V}{c} \quad (6.1)$$

In order to validate subsonic compressible flow for two cases were chosen as outlined in Table 6.1. The airfoil has a length of 1.0089[m] instead of the standard 1[m] in order to give a zero thickness at the trailing edge without changing the airfoil profile otherwise. These larger Mach numbers necessitate including compressibility effects. In order to validate, the results are compared to R.C. Lock's report for the Advisory Group for Aerospace Research and Development [3]. Both cases studied here were calculated by Lock using the finite difference method of C.C.L. Sells [4]. All test cases for the full potential solver were run on using an Intel® i7-3770 processor. The specifications are outlined in Table 6.2.

Table 6.1: Subsonic Compressible Test Cases

Case	Airfoil	$\alpha [^\circ]$	$M_\infty [-]$	Chord length [m]
(1)	NACA0012	0.0	0.72	1.0089
(2)	NACA0012	2.0	0.63	1.0089

Table 6.2: Specifications of Intel® i7-3770 Processor [2]

Specifications	
Number of cores	4
Number of threads	8
Processor Base Frequency	3.40 GHz
Cache	8 MB Intel® Smart Cache
Bus Speed	5 GT/s

6.1 Mesh Refinement

Finite-element results must be independent of the mesh, and for this reason a mesh refinement study should be conducted. The finite-element solver is tested with various mesh sizes to test both the convergence of the solution and the reaction to the changes in mesh size. The mesh sizes for this convergence study range from sizes of $1E-1$ to $1E-8$. A domain size of $100[m] \times 100[m]$ was used for every case. The results should also be independent of the domain size which is discussed in Section 6.2.

6.1.1 Verification

Figures 6.1, 6.2, 6.3, 6.4 show the distribution of the velocity and the pressure coefficient for one of the considered mesh sizes. Figures 6.5 and 6.6 illustrate the mesh refinement process. In order to evaluate the results the resulting lift coefficient from the simulations was compared to the lift coefficient found by data from Lock [3], where the lift is listed as 0 for $\alpha = 0.0^\circ$ and 0.335 for $\alpha = 2.0^\circ$. The relative error found for the various mesh sizes can be seen in Fig. 6.7. For $\alpha = 0.0^\circ$, seen in Fig. 6.10a, the error is low for all presented mesh sizes, however with a mesh size of 10^{-3} a relative error of 0.0094 can already be achieved. For $\alpha = 2.0^\circ$, seen in Fig. 6.10b, the errors are larger than for the first case. With a mesh size of 10^{-3} an error of 1.601953 was achieved. However, this is still considered acceptable. Therefore, both cases provide reasonable errors and convergence with mesh refinement. All numerical results can be seen in Tables 6.3 and 6.4.

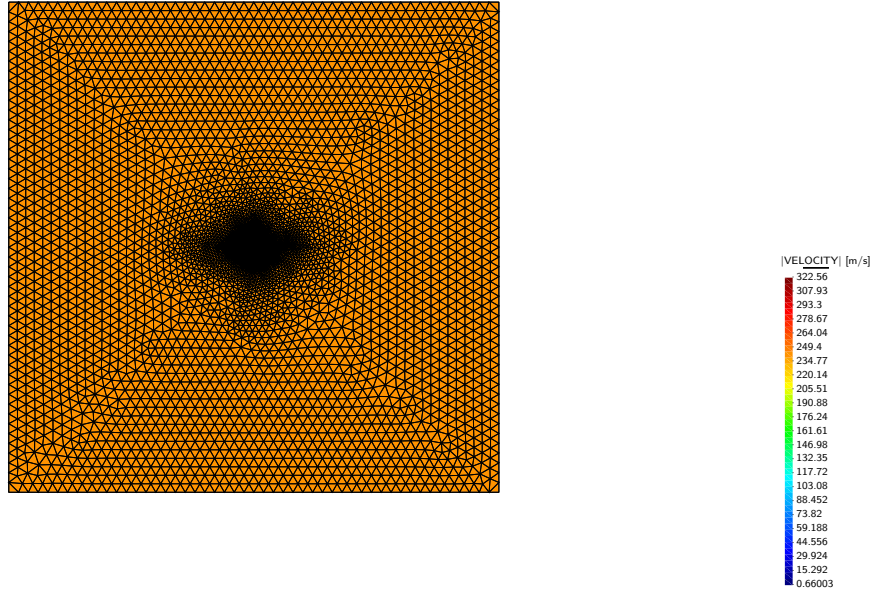


Figure 6.1: Magnitude of Velocity Over Entire Domain for $\alpha = 0.0^\circ$, Airfoil Mesh Size $1e-4$

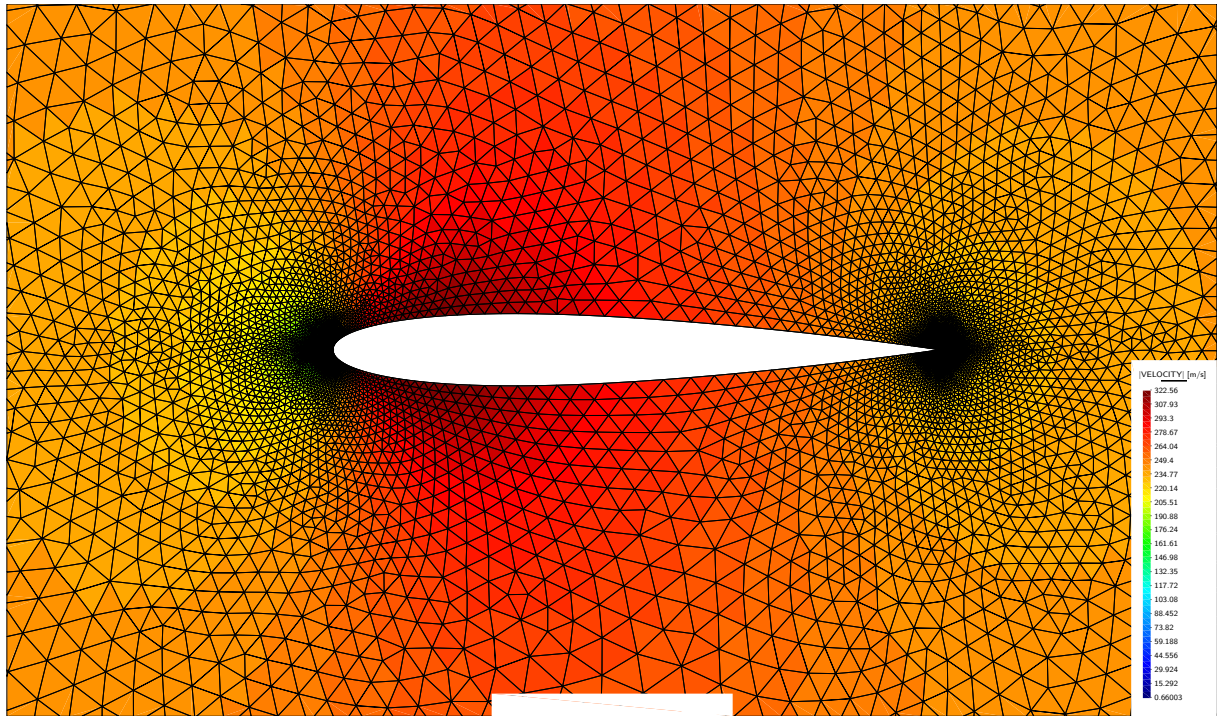


Figure 6.2: Magnitude of Velocity Next to Airfoil for $\alpha = 0.0^\circ$, Airfoil Mesh Size $1e-4$

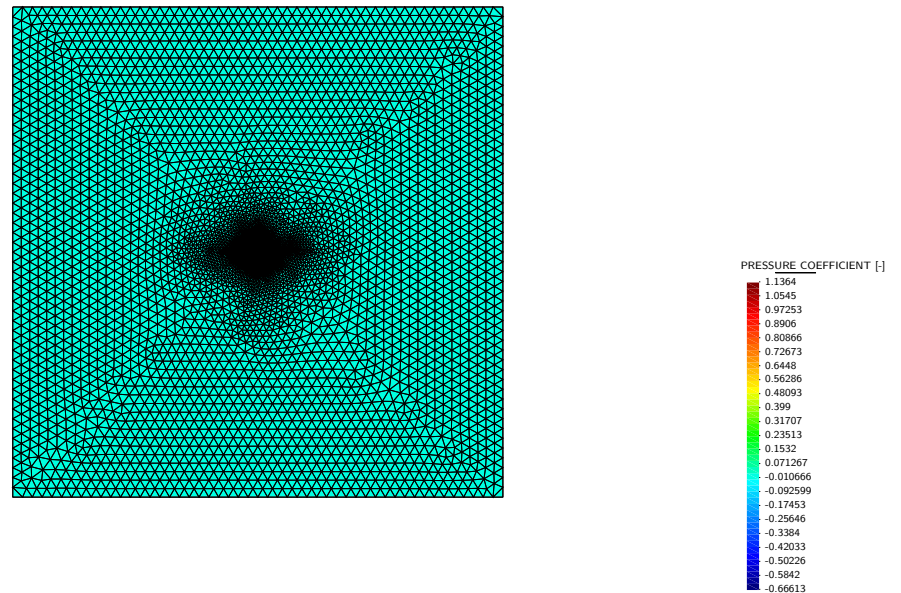


Figure 6.3: Pressure Coefficient Over Entire Domain for $\alpha = 0.0^\circ$, Airfoil Mesh Size $1e-4$

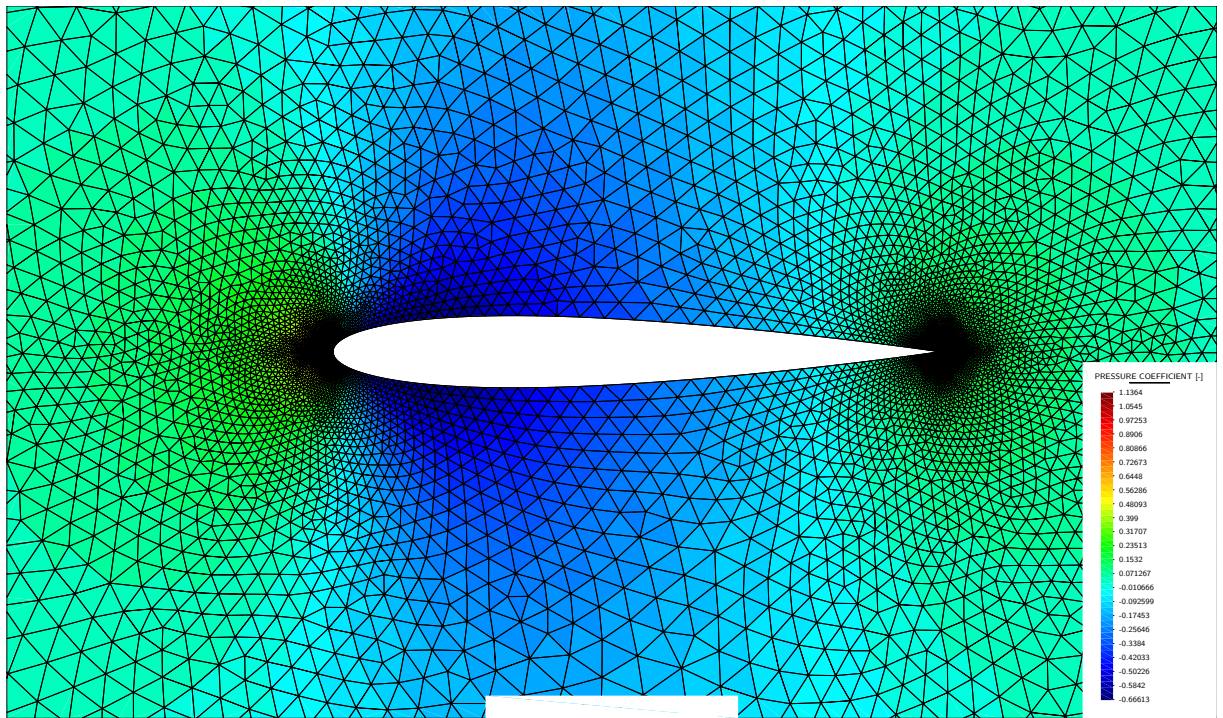


Figure 6.4: Pressure Coefficient Close to Airfoil for $\alpha = 0.0^\circ$, Airfoil Mesh Size 1e-4

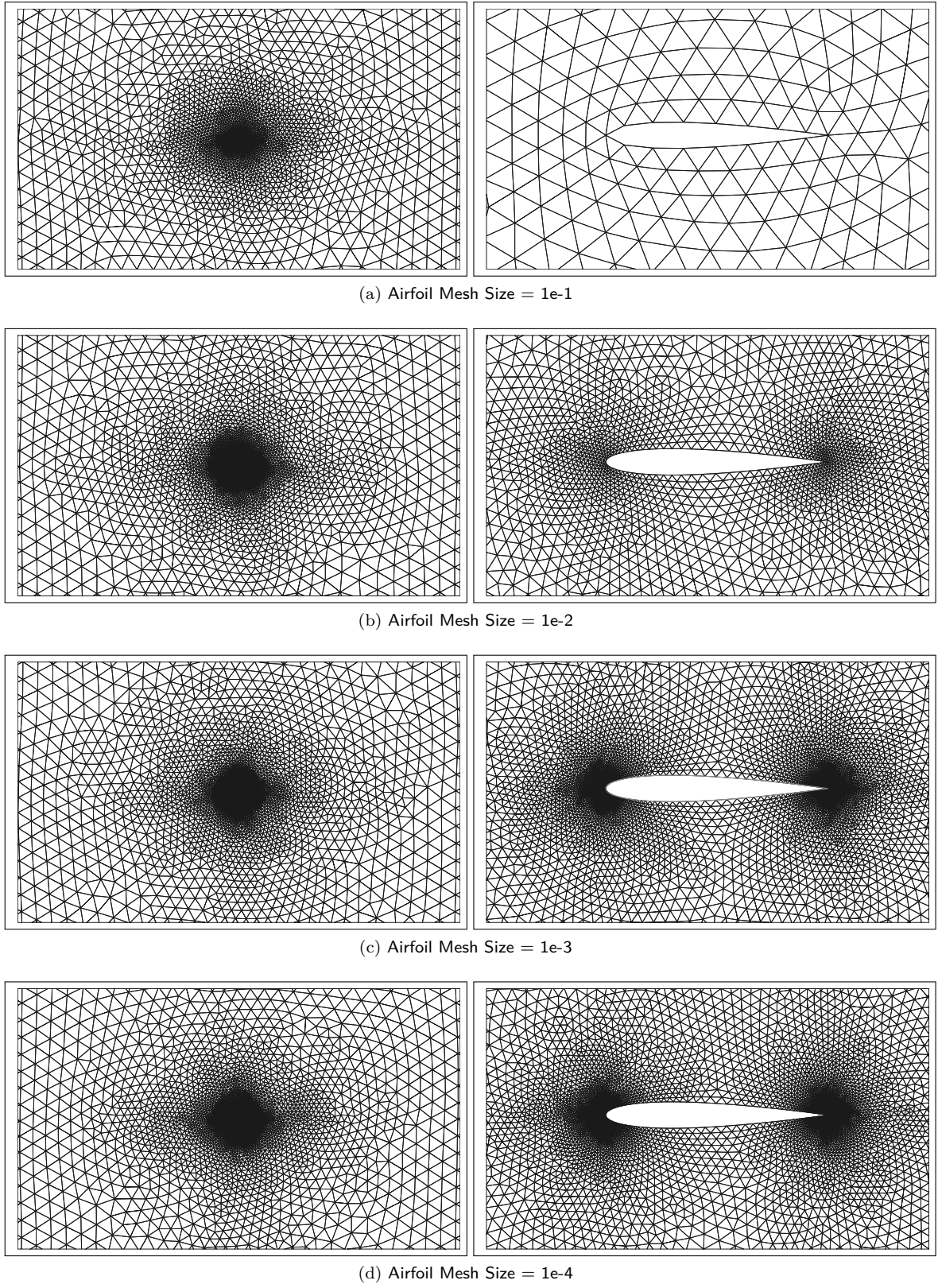


Figure 6.5: Meshes around NACA 0012, $\alpha = 0.0^\circ$

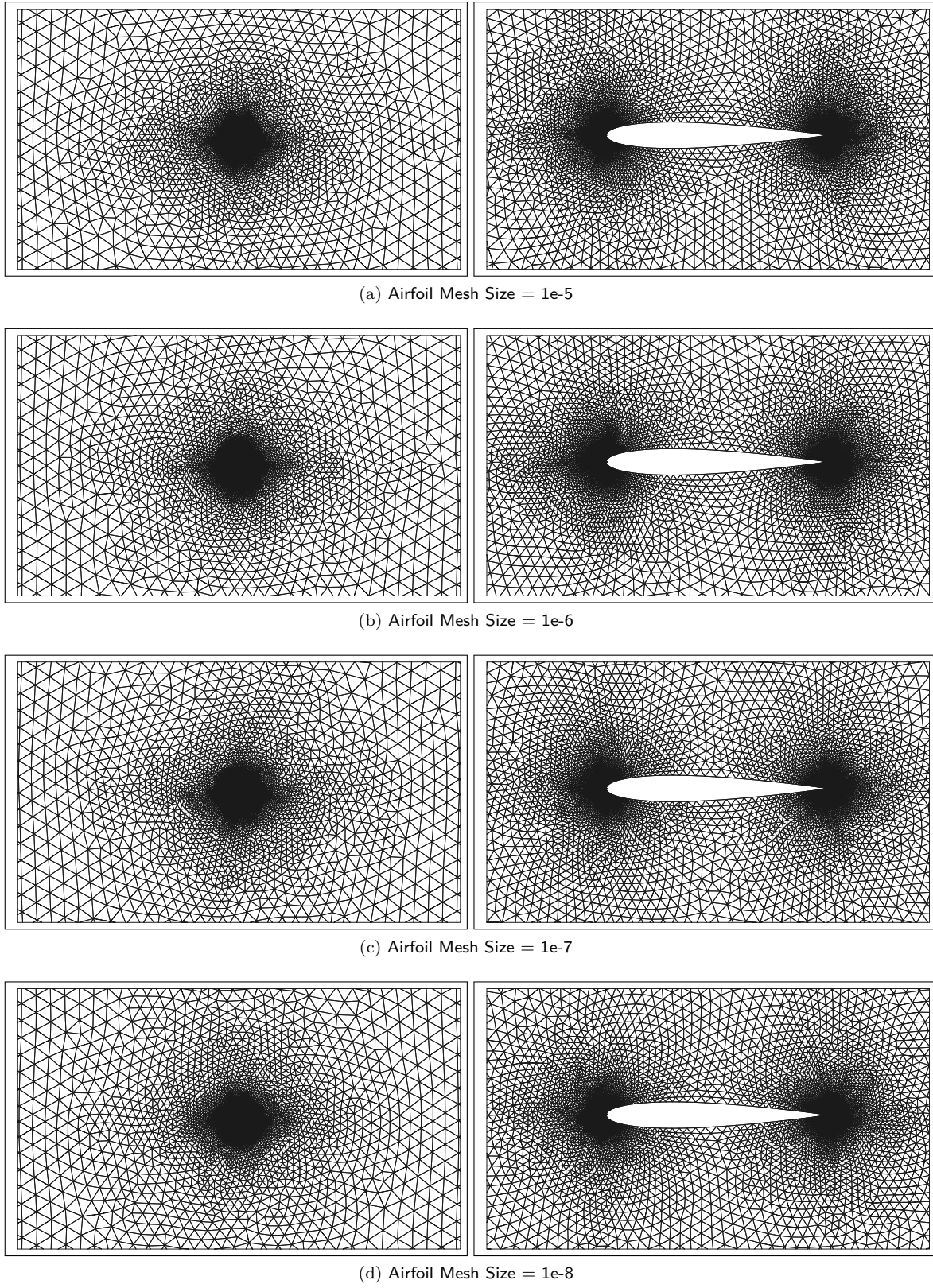


Figure 6.6: Meshes around NACA 0012, $\alpha = 0.0^\circ$

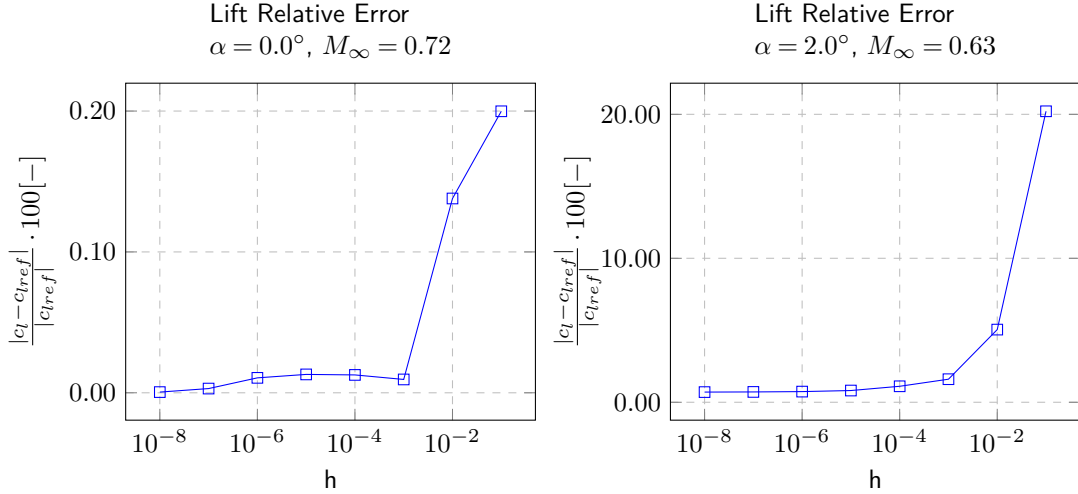


Figure 6.7: Relative Error in Lift Coefficient in Both Mesh Studies

 Table 6.3: Mesh refinement study (NACA 0012, $\alpha = 0^\circ, M_\infty = 0.72$).

Airfoil Mesh Size	#Nodes	$c_l [-]$	$c_d [-]$	Solving time [s]	#Airfoil Nodes
1e-1	4750	-0.001998	0.002136	0.9494838	16
1e-2	7866	0.001379	-0.000218	0.2422657	76
1e-3	11788	0.000095	-0.000015	0.35470691	166
1e-4	15251	-0.000127	-0.000009	0.48192464	262
1e-5	18684	0.000130	-0.000013	0.67006336	360
1e-6	21951	0.000106	-0.000010	0.6210135	456
1e-7	25174	-0.000030	-0.000009	0.7247814	552
1e-8	26656	0.000005	-0.000013	0.7793043	648

 Table 6.4: Mesh refinement study (NACA 0012, $\alpha = 2^\circ, M_\infty = 0.63$).

Airfoil Mesh Size	#Nodes	$c_l [-]$	$c_d [-]$	Solving time [s]	#Airfoil Nodes
1e-1	4785	0.267290	0.004223	0.22636484	16
1e-2	8168	0.318092	-0.000142	0.32949807	76
1e-3	11752	0.329633	0.000006	0.41735864	166
1e-4	15239	0.331282	0.000010	0.55490383	262
1e-5	18566	0.332271	0.000006	0.64397189	360
1e-6	21876	0.332519	0.000009	0.7167151	456
1e-7	24839	0.332597	0.000015	0.8535662	552
1e-8	26824	0.332632	0.000007	0.9188675	648

6.1.2 Validation

In order to see how well the full potential solver represents the physical system the pressure coefficient distributions were also considered against the results presented by Lock [3]. In Fig. 6.8 the pressure coefficient distribution for various mesh sizes is displayed. There is good matching between the results presented by Lock for the $\alpha = 0.0^\circ$ case. In Fig. 6.9 the pressure coefficient can be seen for the $\alpha = 2.0^\circ$ case can be seen. Here there is also good matching between the Lock data and the full potential solution.

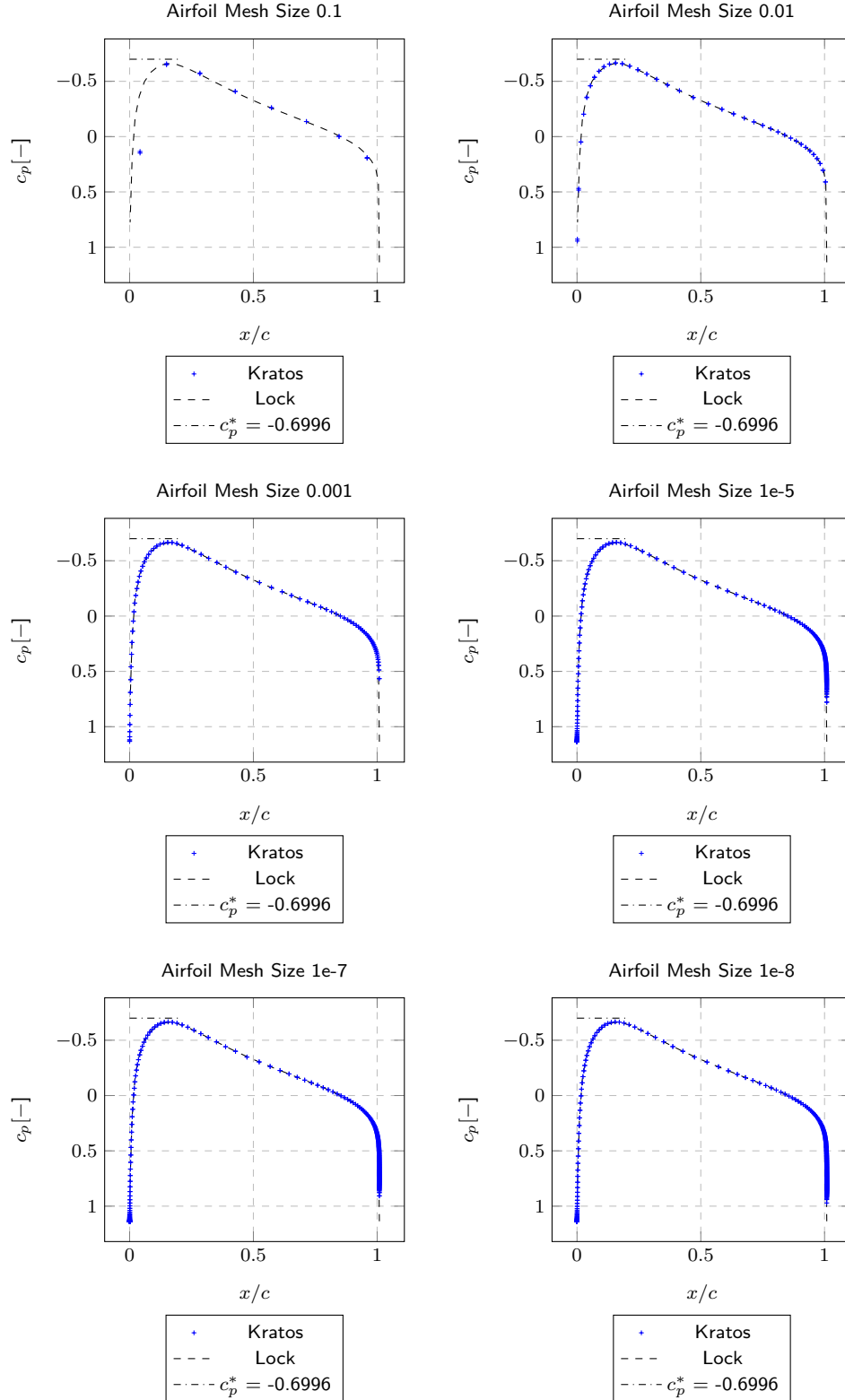


Figure 6.8: Pressure coefficient distribution. $\alpha = 0.0^\circ$, $M_\infty = 0.72$, Domain Size of 100

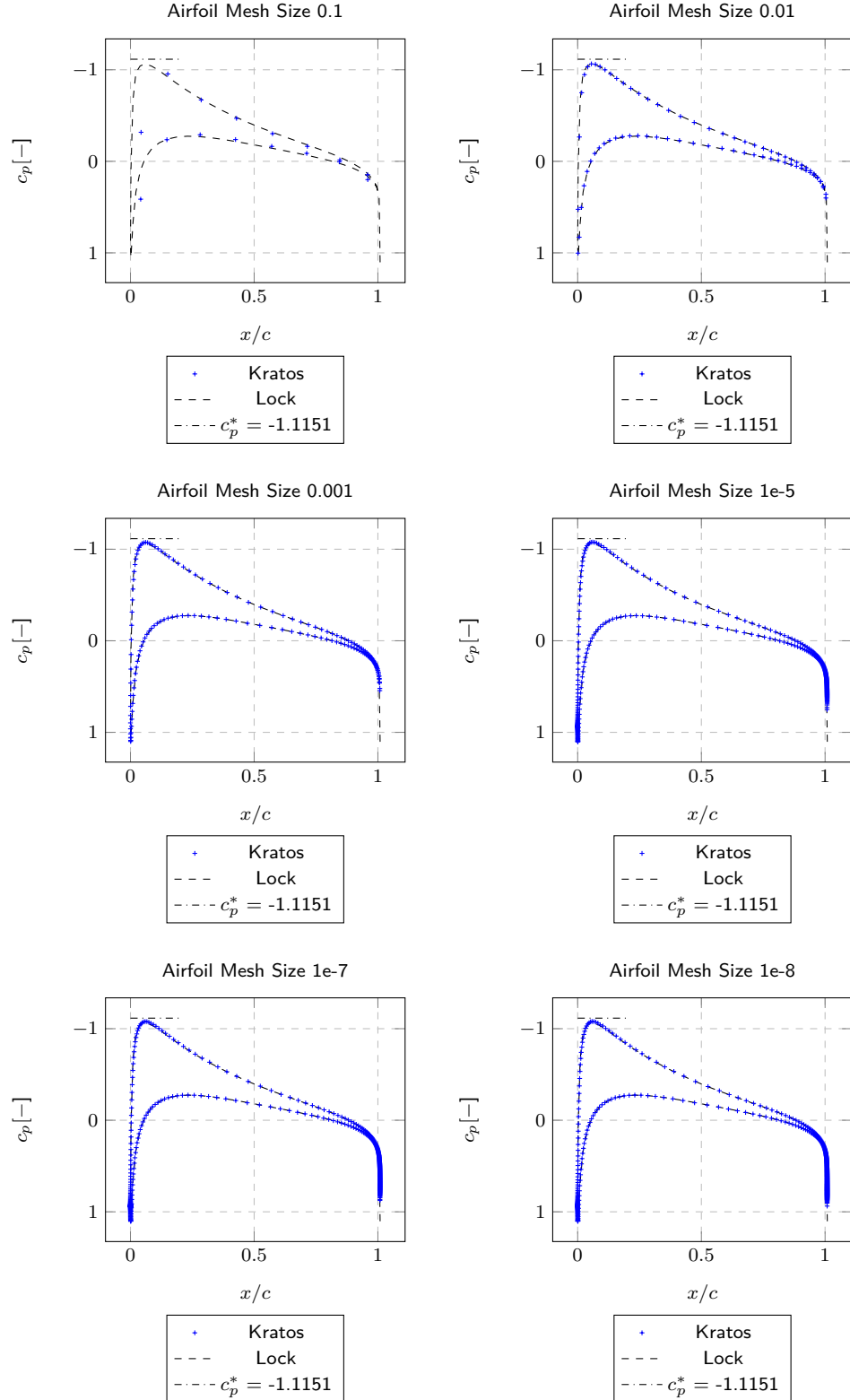


Figure 6.9: Pressure coefficient distribution. $\alpha = 2.0^\circ$, $M_\infty = 0.63$, Domain Size 100

6.2 Domain Study

6.2.1 Verification

Domain sizes between $1e2$ to $1e5$ were tested with mesh sizes between $1e-3$ and $1e-6$. The effect on the mesh in changing the size of the domain for the largest mesh size can be seen in Fig. 6.11. Then the convergence of the lift coefficient for the various domain sizes for the smallest mesh size can be seen in Fig. 6.10. All the numerical results can be seen in Tables 6.5 and 6.4.

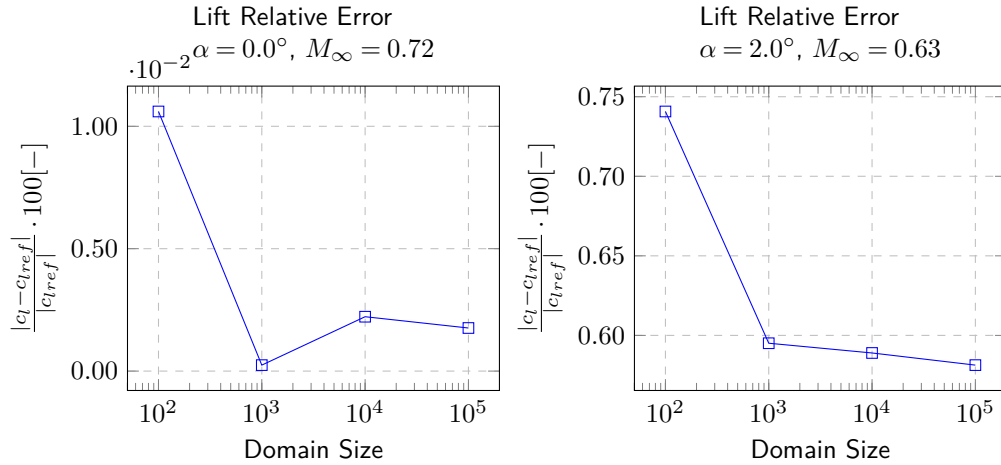


Figure 6.10: Relative Error in Lift Coefficient in Both Mesh Studies, Airfoil Mesh Size $1e - 6$

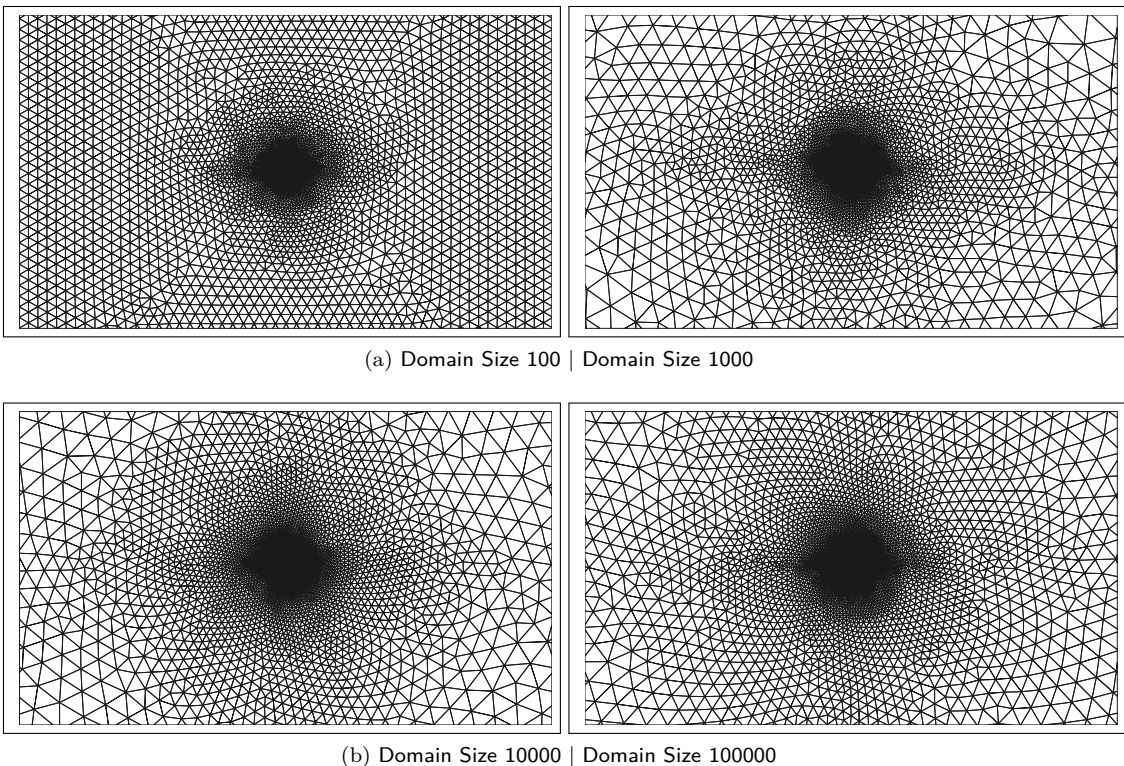


Figure 6.11: Meshes around NACA 0012, $\alpha = 0.0^\circ$, Airfoil Mesh Size = $1e-3$

Table 6.5: Domain size study (NACA 0012, $\alpha = 0^\circ$, $M_\infty = 0.72$).

Domain Size	Airfoil Mesh Size	#Nodes	$c_l [-]$	$c_d [-]$	Solving time [s]	#Airfoil Nodes
1e2	1e-3	11788	0.000095	-0.000015	0.44945709	166
1e2	1e-4	15251	-0.000127	-0.000009	0.5852625	262
1e2	1e-5	18684	0.000130	-0.000013	0.6540213	360
1e2	1e-6	21951	0.000106	-0.000010	0.7343903	456
1e3	1e-3	14074	0.000026	-0.000029	0.57762896	166
1e3	1e-4	17714	0.000090	-0.000007	0.6010877	262
1e3	1e-5	21159	-0.000089	-0.000012	0.7163748	360
1e3	1e-6	24114	-0.000002	-0.000006	0.8029968	456
1e4	1e-3	16462	0.000021	-0.000019	0.593327	166
1e4	1e-4	20138	0.000092	-0.000014	0.6819112	262
1e4	1e-5	23323	0.000038	-0.000008	0.8146724	360
1e4	1e-6	26603	-0.000022	-0.000008	0.9094603	456
1e5	1e-3	19187	-0.000224	-0.000024	0.646301	166
1e5	1e-4	22382	-0.000041	-0.000017	0.7261533	262
1e5	1e-5	25742	0.000193	-0.000000	0.8724467	360
1e5	1e-6	28819	0.000018	-0.000004	1.0301166	456

 Table 6.6: Domain size study (NACA 0012, $\alpha = 2^\circ$, $M_\infty = 0.63$).

Domain Size	Airfoil Mesh Size	#Nodes	$c_l [-]$	$c_d [-]$	Solving time [s]	#Airfoil Nodes
1e2	1e-3	11752	0.329633	0.000006	0.44551014	166
1e2	1e-4	15218	0.331289	0.000009	0.56315268	262
1e2	1e-5	18566	0.332271	0.000006	0.6295732	360
1e2	1e-6	21876	0.332519	0.000009	0.7254988	456
1e3	1e-3	14235	0.328473	-0.000013	0.4824868	166
1e3	1e-4	17364	0.331783	-0.000007	0.6243757	262
1e3	1e-5	20766	0.332755	-0.000008	0.6751451	360
1e3	1e-6	24074	0.333007	-0.000009	0.8138628	456
1e4	1e-3	16352	0.328715	-0.000020	0.4742049	166
1e4	1e-4	19888	0.332083	-0.000004	0.6600093	262
1e4	1e-5	23107	0.332808	-0.000011	0.6495238	360
1e4	1e-6	26360	0.333027	-0.000014	0.7344177	456
1e5	1e-3	18708	0.326976	-0.000023	0.5254146	166
1e5	1e-4	22627	0.332296	-0.000015	0.6191256	262
1e5	1e-5	25597	0.332704	-0.000002	0.7139304	360
1e5	1e-6	28672	0.333053	-0.000006	0.8354212	456

6.2.2 Validation

In order to validate the results of the domain study the pressure coefficient distribution is compared to the AGARD data once again. There is a close correlation between the AGARD data and the results of the full potential solver for all cases.

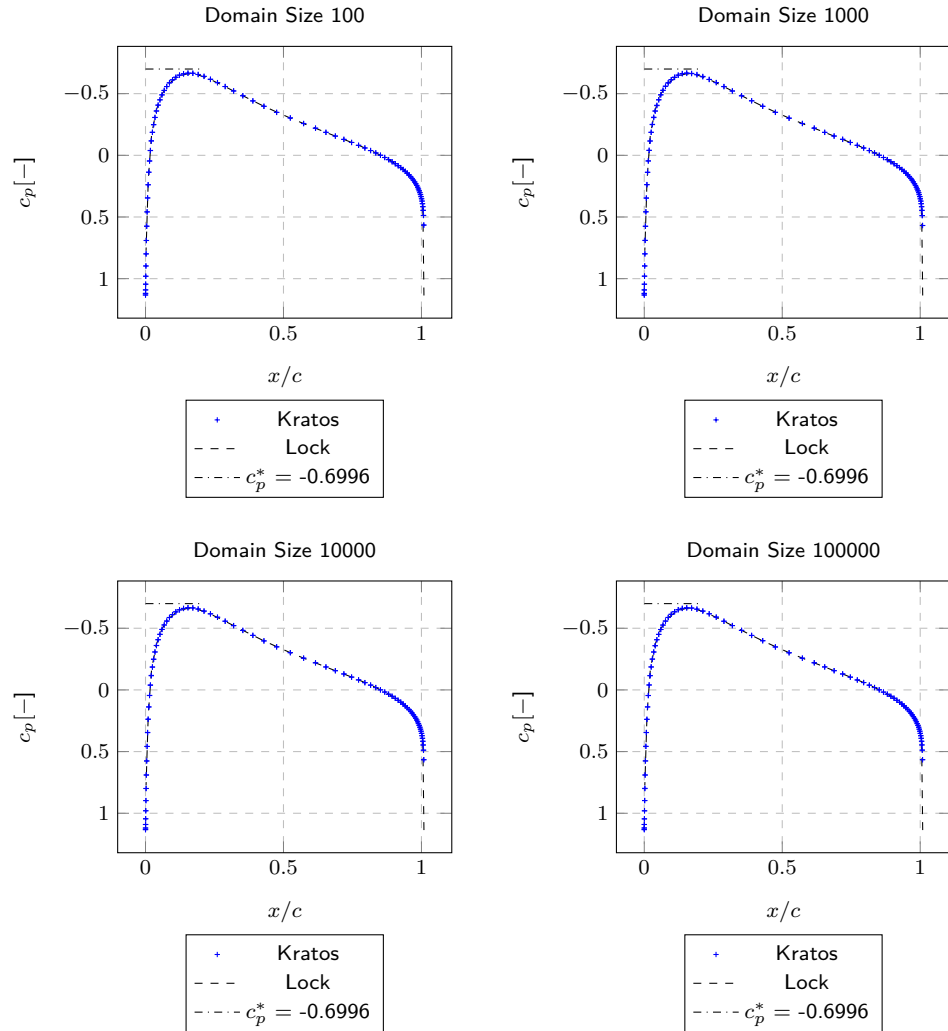


Figure 6.11: Pressure coefficient distribution. $\alpha = 0.0^\circ$, $M_\infty = 0.72$, Airfoil Mesh Size 0.001

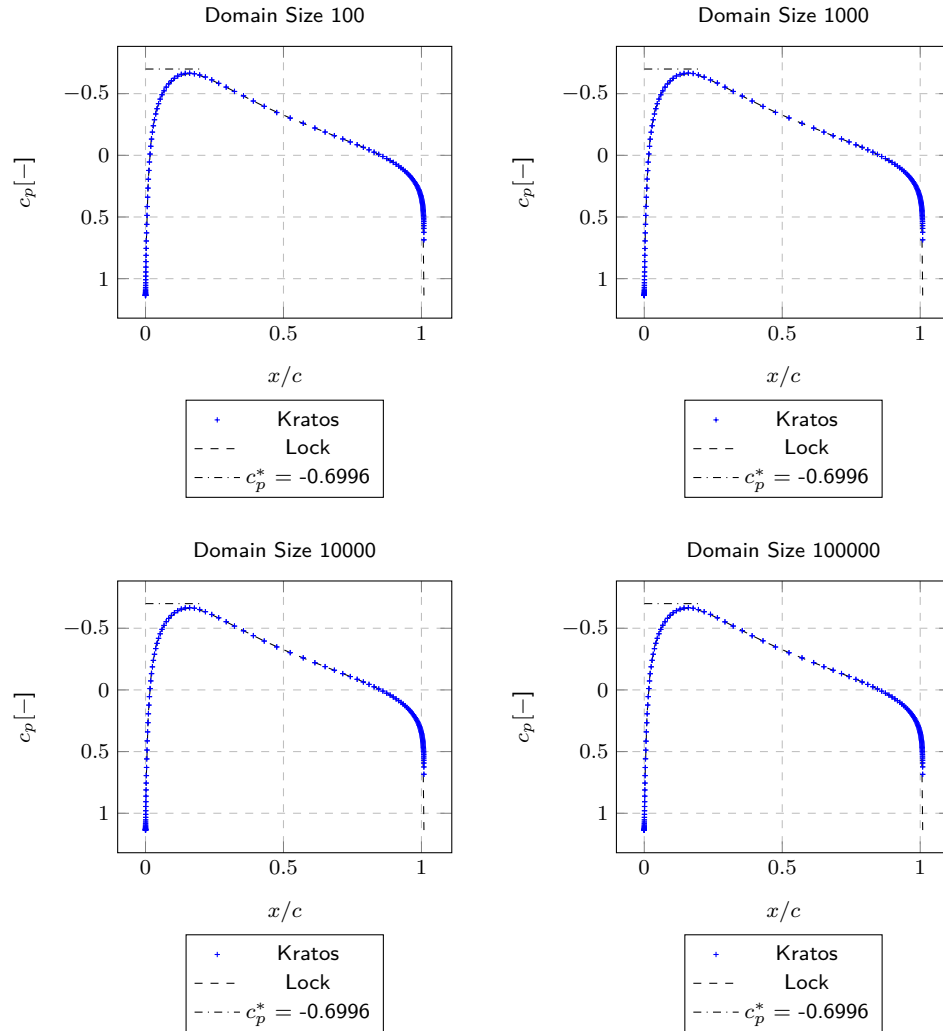


Figure 6.11: Pressure coefficient distribution. $\alpha = 0.0^\circ$, $M_\infty = 0.72$, Airfoil Mesh Size 0.0001

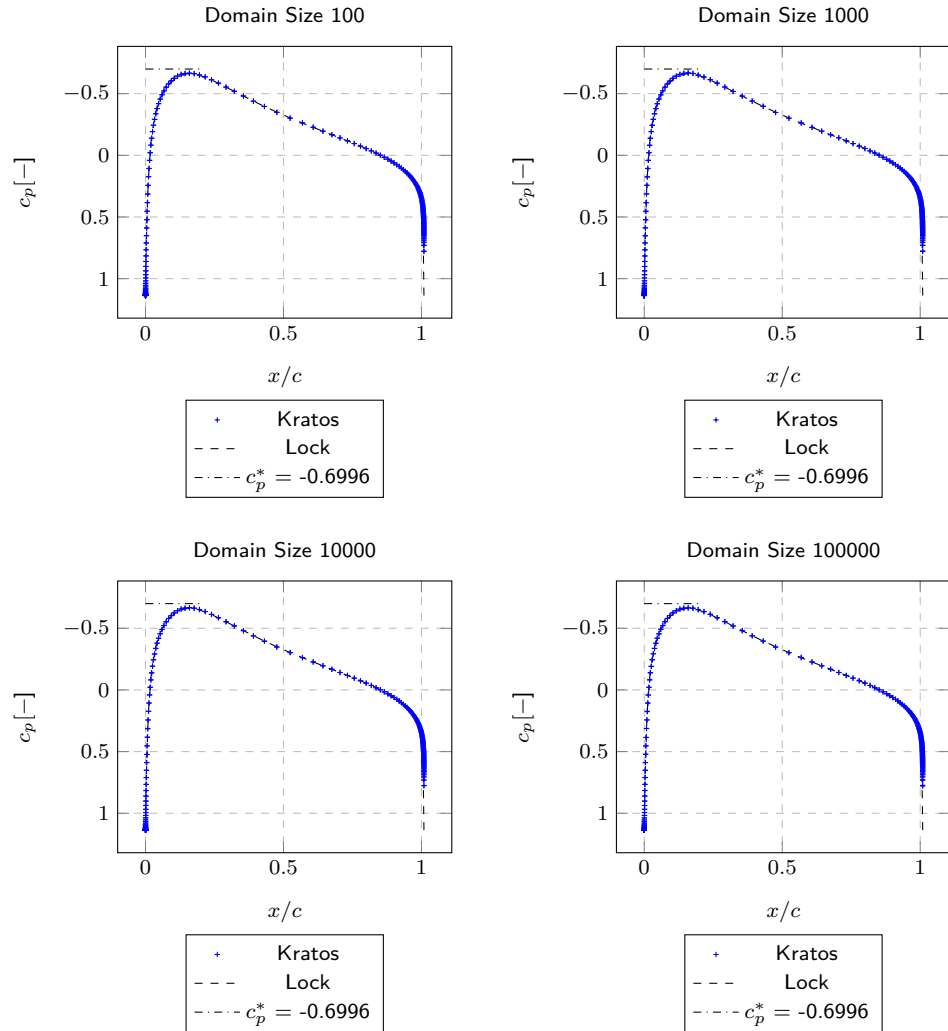


Figure 6.11: Pressure coefficient distribution. $\alpha = 0.0^\circ$, $M_\infty = 0.72$, Airfoil Mesh Size $1e-5$

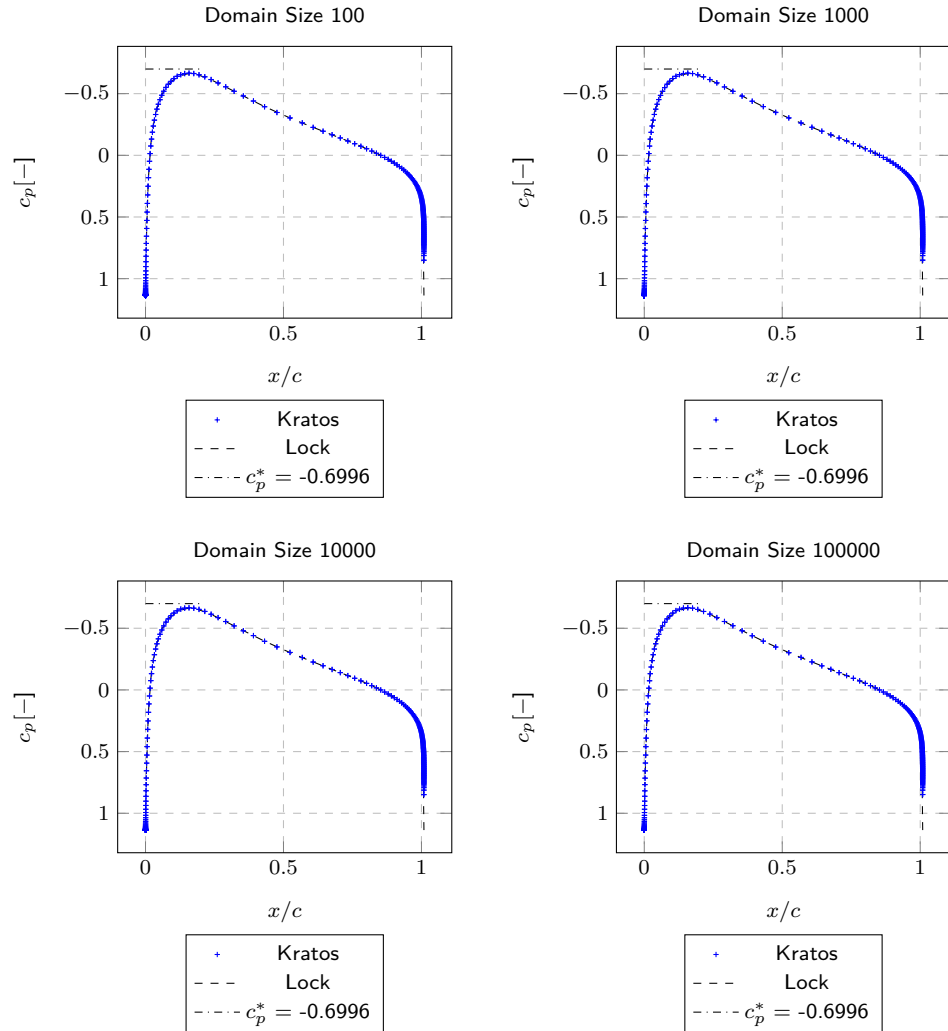


Figure 6.11: Pressure coefficient distribution. $\alpha = 0.0^\circ$, $M_\infty = 0.72$, Airfoil Mesh Size $1e-6$

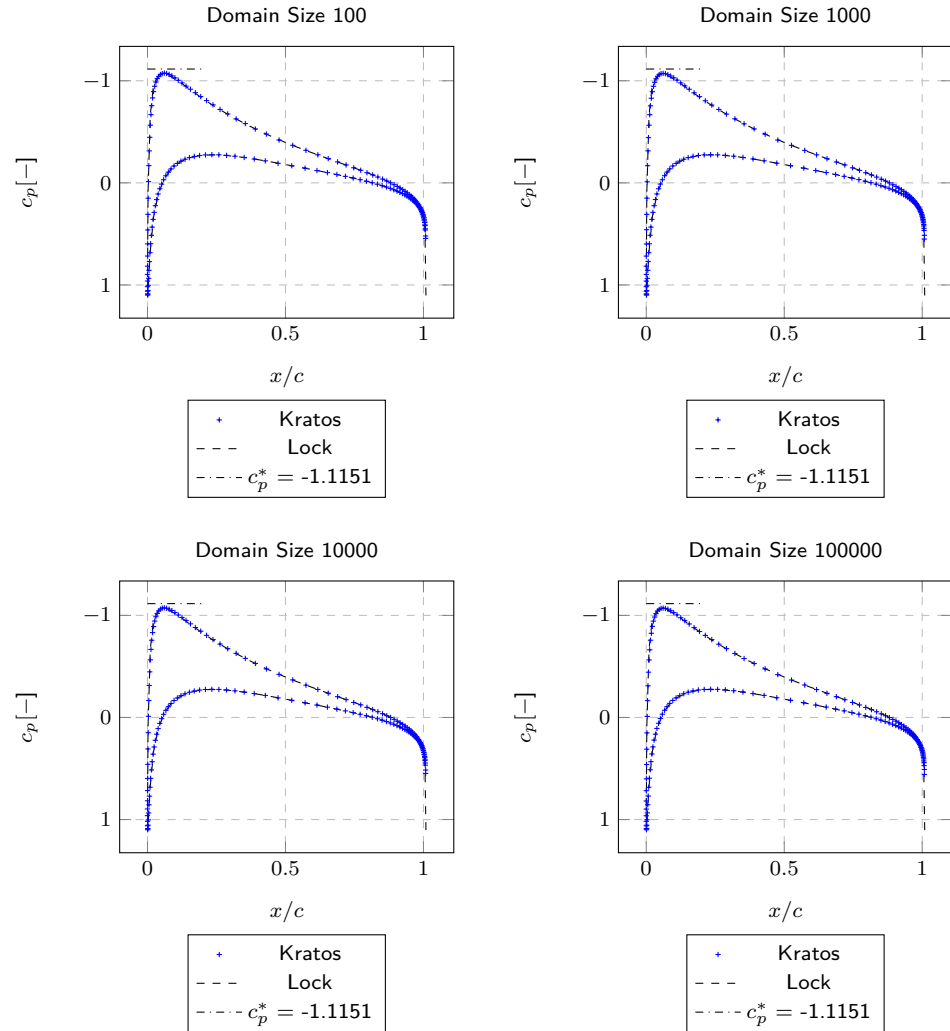


Figure 6.12: Pressure coefficient distribution. $\alpha = 2.0^\circ$, $M_\infty = 0.63$, Domain Size 100

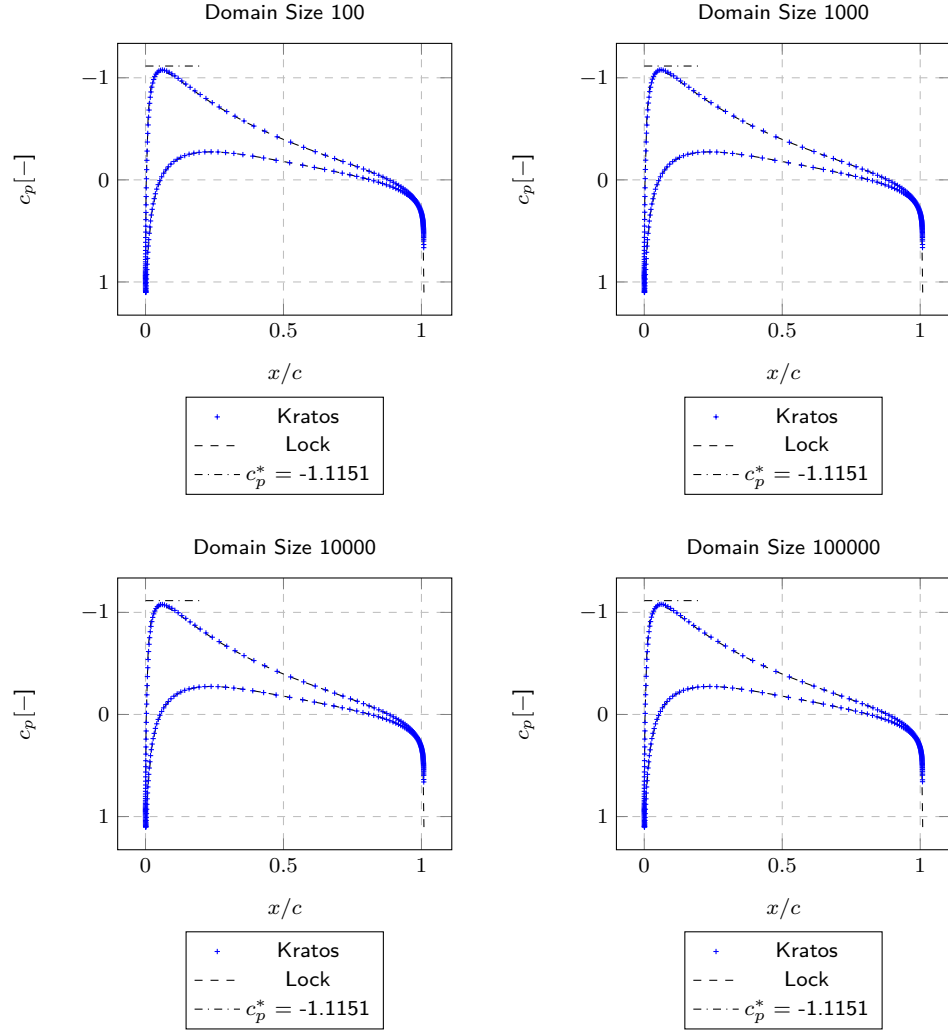


Figure 6.13: Pressure coefficient distribution. $\alpha = 2.0^\circ$, $M_\infty = 0.63$, Domain Size 1000

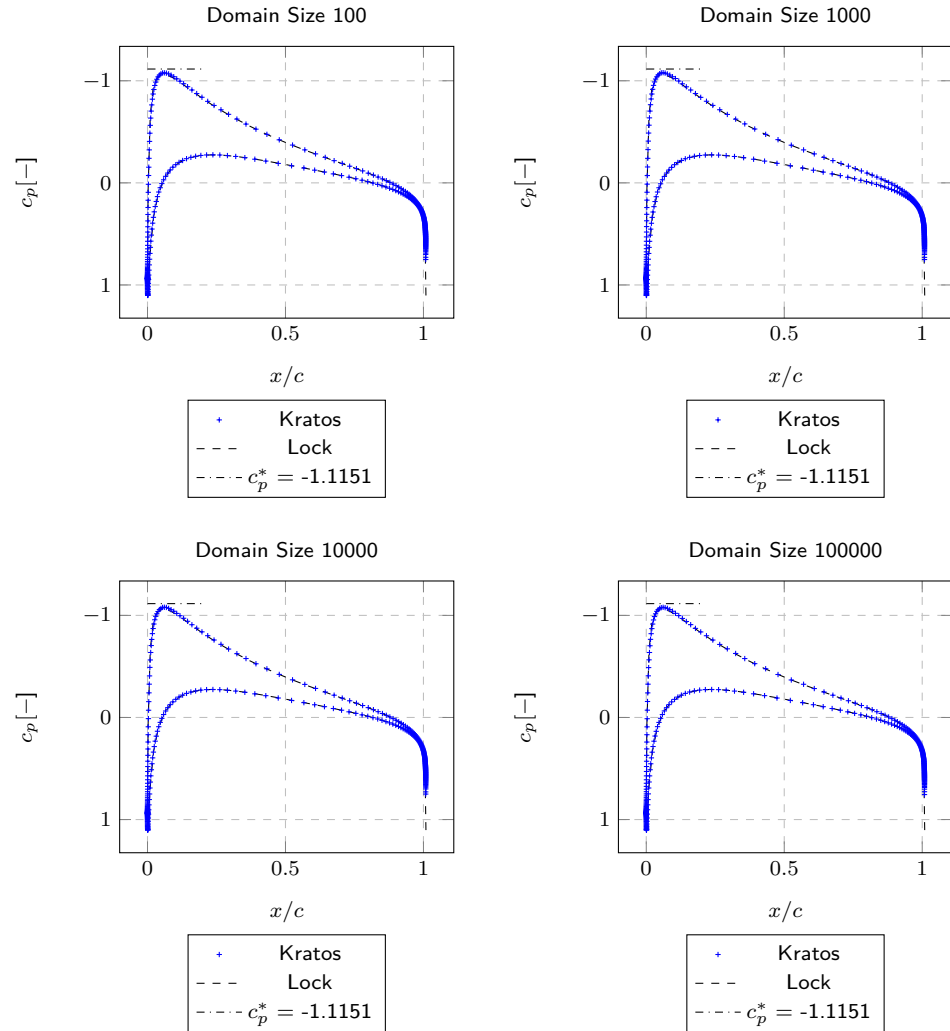


Figure 6.14: Pressure coefficient distribution. $\alpha = 2.0^\circ$, $M_\infty = 0.63$, Domain Size 10000

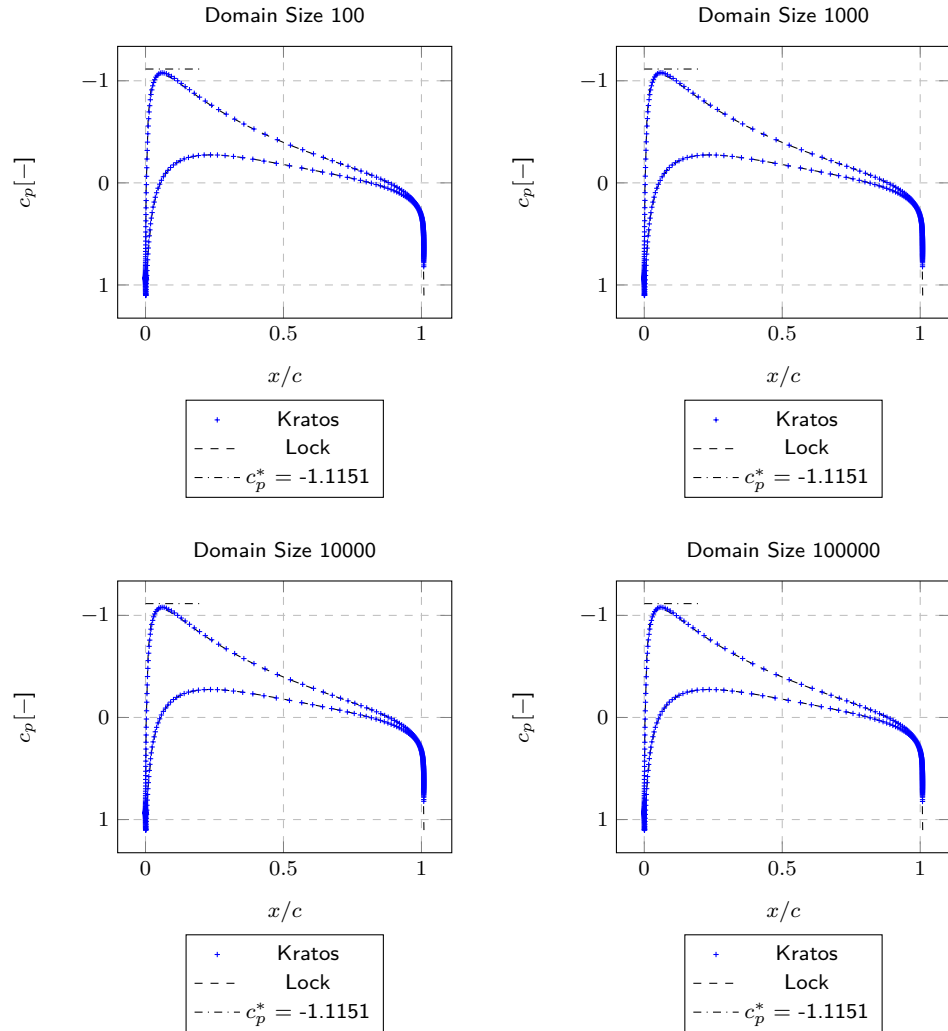


Figure 6.15: Pressure coefficient distribution. $\alpha = 2.0^\circ$, $M_\infty = 0.63$, Domain Size 100000

7 Validation and Verification of Transonic Compressible Potential Flow

8 Conclusions

8.1 Summary

8.2 Outlook

Appendix

Boundary Layer Equations

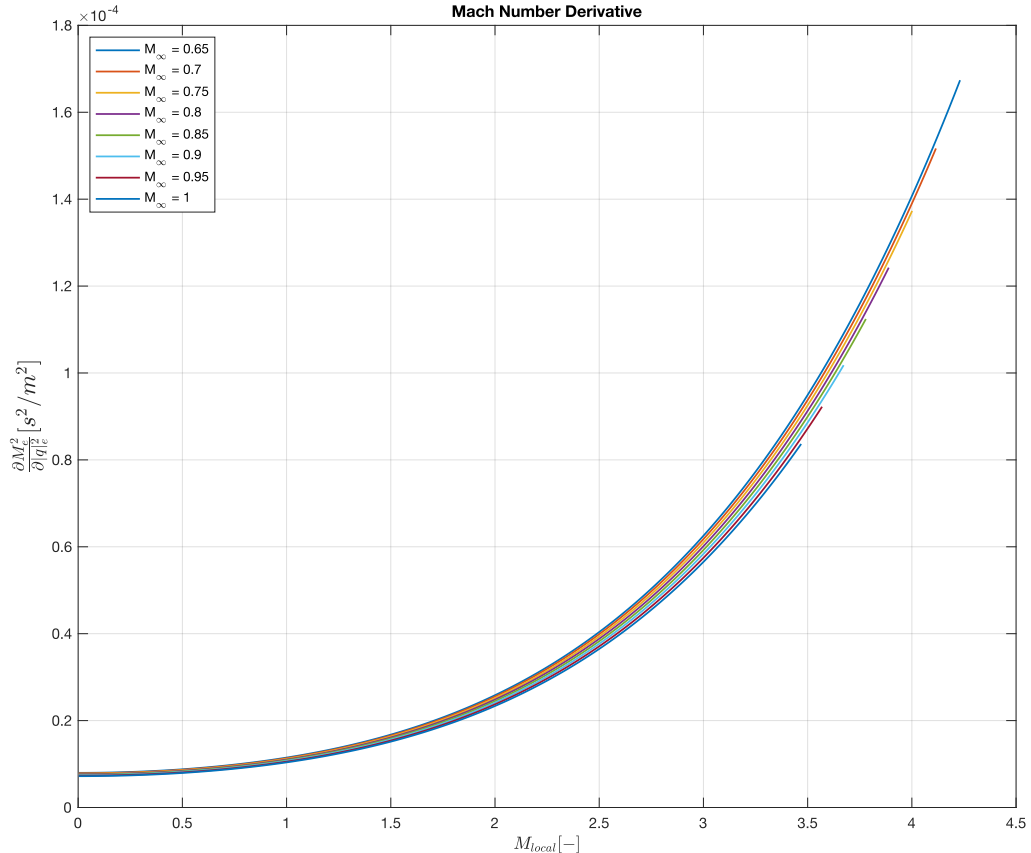


Figure .1: Variation of Mach Number Derivative with Local Mach Number

Bibliography

- [1] M. Drela.
Flight Vehicle Aerodynamics.
The MIT Press, 2014.
- [2] Intel.
Accessed: 2020-03-19.
- [3] R.C. Lock.
AGARD REPORT No. 575 on Test Cases for Numerical Methods in Two-Dimensional Transonic Flow.
Tech. rep.
North Atlantic Treaty Organization Advisory Group for Aerospace Research and Development, 1970.
- [4] C.C.L. Sells.
“Plane subcritical flow past a lifting aerofoil”.
In: *Proceedings of the Royal Society of London. Series A, Mathematical and Physical Sciences* 308 (1969), pp. 377–401.

Declaration

I hereby declare that the thesis submitted is my own unaided work. All direct or indirect sources used are acknowledged as references. In addition, I declare that I make the present work available to the Chair of Structural Analysis for academic purposes and in this connection also approve of dissemination for academic purposes.

Eloisa Baez Jones

Munich, May 8, 2020